# VICTORIA UNIVERSITY
MELBOURNE AUSTRALIA

Mixing of a cylindrical gravity current in a stratified ambient

This is the Published version of the following publication

Lam, Wai Kit, Chan, Leon, Cao, Yicheng, Sutherland, Duncan, Manasseh, Richard, Moinuddin, Khalid and Ooi, Andrew (2024) Mixing of a cylindrical gravity current in a stratified ambient. International Journal of Heat and Fluid Flow, 107. ISSN 0142-727X
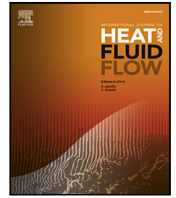
Mixing of a cylindrical gravity current in a stratified ambient

Wai Kit Lam [a],[*], Leon Chan [a], Yicheng Cao [a], Duncan Sutherland [b], Richard Manasseh [c], Khalid Moinuddin [d], Andrew Ooi [a]

[a] *Department of Mechanical Engineering, The University of Melbourne, Parkville, VIC 3010, Australia, Melbourne, 3010, Victoria, Australia*
[b] *School of Science, University of New South Wales, Canberra, ACT 2610, Australia, Canberra, 2610, Australian Capital Territory, Australia*
[c] *Department of Mechanical and Product Design Engineering, Swinburne University of Technology, John St, Hawthorn VIC 3122, Australia, Melbourne, 3122, Victoria, Australia*
[d] *Institute of Sustainable Industries and Liveable Cities, Victoria University, Melbourne VIC 3030, Australia, Melbourne, 3030, Victoria, Australia*

ARTICLE INFO

ABSTRACT

Simulation results from direct numerical simulations (DNSs) of cylindrical gravity currents propagating into a linearly stratified ambient with stratification strengths ranging from 0 to 0.8, at a moderate Reynolds number of Re = 3450 are presented. The simulations are based on the incompressible Navier–Stokes equations, assuming small density differences such that the Boussinesq approximation is valid. The density of the ambient fluid increases linearly from the top (ρ_0) to the bottom (ρ_b) of the domain. A comparative analysis is conducted between the stratified cases and the unstratified case to investigate the impact of ambient stratification strength on the mixing behaviour of cylindrical gravity currents. The energy conversion processes are analysed using the mechanical framework proposed by Winters et al. (1995). The energy budget is formulated by considering gravitational available potential energy, and the evolution of potential energy due to reversible stirring and irreversible diapycnal mixing in the system. The findings reveal a decrease in available potential energy and kinetic energy with increasing stratification strength, indicating lower energy exchange for gravity currents propagating in the stratified environment. Instantaneous and cumulative mixing efficiency calculations during the slumping phase indicate that Kelvin–Helmholtz billow play an important role in stirring the heavy fluid and causing irreversible mixing with the ambient fluid.

1. Introduction

Gravity currents or density currents are a horizontal intrusion of a fluid of a (usually) higher density into an ambient fluid. Gravity currents are observed in many naturally occurring phenomena such as sandstorms (Parsons, 2000), powder-snow avalanches (Turnbull and McElwaine, 2007), and bushfires (Dold et al., 2006). Comprehensive reviews of gravity currents in geophysical flows, laboratory experiments and numerical simulations can be found in Simpson (1982) and Meiburg et al. (2015).

We consider a body of heavy fluid initially at rest released into an ambient at $t = 0$. The heavy fluid collapses and leads to an intrusion of fluid with a distinct head region. Numerous studies have extensively investigated the dynamics of gravity currents in both (two-) three-dimensional planar and (axisymmetric) cylindrical configurations (without any stratification in the ambient fluid), employing both experimental (Marino et al., 2005; Huppert and Simpson, 1980; Alahyari and Longmire, 1996) and numerical (Blanchette et al., 2005; Cantero et al., 2007b,a, 2008) approaches. The studies have revealed that the

propagation of the gravity current goes through four distinct stages. Initially, the gravity current undergoes an acceleration phase (zero to maxima) after the release of the heavy fluid, where the gravitational potential energy of the dense fluid is converted into kinetic energy. Once the front velocity reaches its maximum, the acceleration phase is followed by the slumping phase, characterised by constant front height and speed. Subsequently, the gravity current transitions into the self-similar inertial phase, where the buoyancy force is balanced by the inertial force. Eventually, the gravity current enters the viscous phase, in which the viscous force becomes dominant over the buoyancy force. During the inertial and viscous phases, the front velocity of the gravity current decays following a power law relationship.

However, the presence of stratification in the ambient can significantly influence the propagation and behaviour of gravity currents, due to the generation of internal waves. Consequently, researchers have conducted experimental and numerical investigations to explore the impact of stratification on the dynamics of gravity current. In this

---

Nomenclature

$(\cdot)^*$	Dimensional variables
ϵ	Local dissipation
η	Kolmogorov microscale
η_m	Mixing efficiency
γ	Density ratio
κ	Molecular diffusivity
Fr	Froude number
Re_L	Local Reynolds number
Re	Reynolds number
Sc	Schmidt number
$\mathscr{M}$	Mixing rate
ν	Kinematic viscosity
$\overline{(\cdot)}$	Spatial averaging variables
Φ_d	Irreversible diapycnal mixing
Φ_i	Irreversible diffusion
Φ_z	Reversible buoyancy flux
ρ_0	Fluid density at the top boundary
ρ_a	Density of the ambient fluid
ρ_b	Fluid density at the bottom boundary
ρ_c	Density of the heavy fluid
$\tilde{z}$	Vertical coordinate in the reference state
g	Gravitational acceleration
$g\prime$	Reduced gravity
H	Depth of the domain
IA	Initial acceleration
IP	Inertial phase
N	Buoyancy frequency
p	Pressure
S	Stratification parameter
s_{ij}	Strain rate tensor
SP	Slumping phase
T	Time scale
U	Velocity scale
u	Velocity component
$u_{f,mean}$	Mean front velocity in the slumping phase
VP	Viscous phase
x	Streamwise coordinate
y	Spanwise coordinate
z	Vertical coordinate

gravity current ($\mathrm{Fr} > 1/\pi$), the gravity current travels faster than the internal gravity wave. Ungarish and Huppert (2002) developed a one-layer inviscid shallow-water approximation and demonstrated excellent agreement with the experimental results reported by Maxworthy et al. (2002).

Early studies related to the energy budget of gravity currents propagating into an unstratified ambient were conducted by Necker et al. (2005) and Birman et al. (2005) using a high-resolution numerical code. Necker et al. (2005) presented a comprehensive investigation of the energy budget and mixing behaviour of three-dimensional, Boussinesq particle-driven gravity current in an unstratified ambient. However, it is important to note that the focus of their study differs from the present study. In their findings, it was observed that approximately 40% of the initial potential energy in the system is 'lost' due to particle settling, resulting in its unavailability for convective transport and mixing. The particle settling introduces additional dissipative losses in the flow and this phenomenon does not occur in density-driven gravity currents investigated here. On the other hand, Birman et al. (2005) conducted an analysis of the energy budget of a two-dimensional, non-Boussinesq, lock exchange flow in an unstratified ambient using spectral and compact finite-difference methods. They reported an increase in the rate of conversion of potential energy to kinetic energy with decreasing density ratio $\gamma = \rho_0/\rho_c$ (where ρ_0 represents the density of the lighter fluid). Ungarish and Huppert (2006, 2008) conducted a study investigating the energy exchange of a 2D planar and an axisymmetric current at high Reynolds numbers, released from a lock and propagating over a horizontal boundary in both unstratified and linearly stratified ambient. They employed both the shallow-water model and Navier–Stokes finite difference simulations and obtained a reasonable agreement in the energy changes of the current between the two approaches. In the case of the axisymmetric current, the energy exchange during the inertial phase was accurately captured using the shallow-water analysis, neglecting the motion in the stratified ambient. The study revealed that stratification enhances the accumulation of potential energy in the ambient and reduces the dissipation of the two-fluid system.

Recently, Dai et al. (2021) conducted experimental and numerical studies on both two- and three-dimensional planar release gravity current in a linearly stratified ambient with varying stratification strength. The energy budgets of the simulations were evaluated by subcritical and supercritical planar gravity currents propagating into a linearly stratified ambient. In the subcritical case, all the energy components showed good agreement between the two- and three-dimensional simulations, except for the dissipation rate. For the supercritical case, the two-dimensional simulations accurately captured the kinetic energy of the current and the potential energy of the ambient are captured but underpredict the dissipation rate. However, the kinetic energy of the ambient and the potential energy of the current are overpredicted and the dissipation rate is underpredicted by the two-dimensional simulations. The discrepancy between the two- and three-dimensional simulations for the supercritical case increased dramatically with increasing stratification strength, highlighting the need for cautious interpretation. In conclusion, Dai et al. (2021) reported that stratification hinders the decay of the total mechanical energy and enhances the accumulation of potential energy in the stratified ambient, which is consistent with the findings of Ungarish and Huppert (2006, 2008).

The energy exchange of two-dimensional planar and axisymmetric gravity currents has been extensively studied in both unstratified and linearly stratified ambient conditions. However, there is limited research on the energy budget of cylindrical release gravity currents in a stratified ambient. Therefore, our focus is on investigating the mixing behaviour of a fully three-dimensional (3D) cylindrical gravity currents as it spreads radially and azimuthally into a linearly stratified ambient. This study is important because cylindrical currents exhibit different characteristics, including higher spreading rates compared to planar currents (Cantero et al., 2007b). Additionally, the presence of

regard, Maxworthy et al. (2002) conducted a comprehensive investigation, utilising both experimental and numerical tools, to analyse the propagation of a saline current released from behind a lock over a horizontal bottom into a rectangular channel with a linearly stratified saline ambient. Their study focused on examining the relationship between the Froude number $\mathrm{Fr} = u_{f,mean}^*/N^*H^*$, where $u_{f,mean}^*$ is the mean front velocity in the slumping phase, $(N^*)^2 = g^*(\rho_b^* - \rho_0^*)/\rho_0^*H^*$ is the buoyancy frequency, g^* is the gravitational acceleration, ρ_0^* is the density at the top of the domain, ρ_b^* is the density at the bottom of the domain and H^* is the depth of the domain and the stratification parameter $S = (\rho_b^* - \rho_0^*)/(\rho_c^* - \rho_0^*)$, where ρ_c^* denotes the density of the heavy fluid. Additionally, they presented data of the critical speed relative to the linear, mode-one, long internal gravity wave, N^*H^*/π, as well as the location at which the first significant interaction between the wave and the nose of the current was observed. Note that in this manuscript, variables with asterisks ($*$) denote dimensional variables. For the subcritical gravity current ($\mathrm{Fr} < 1/\pi$), the internal gravity wave travels faster than the current, whereas for the supercritical

stratified ambient can significantly influence the propagation of the current, as indicated by previous studies conducted by Birman et al. (2007), Lam et al. (2018a,b), Dai et al. (2021), Lam et al. (2022b,a, 2024) and Zahtila et al. (2024).

This study aims to investigate the effects of the strength of stratification, S on the mixing of the cylindrical release gravity current flow on the horizontal plane at a moderate Reynolds number Re = 3450 based on the height of the domain and the velocity scale (see Eq. (5)). The choice of this Reynolds number is based on the study conducted by Cantero et al. (2007b), who performed three-dimensional simulations of cylindrical gravity currents in an unstratified ambient. We describe the formulation of the problem in Section 2. In Section 3, we describe the energy budget method. The quantitative results are presented in Section 4. Finally, conclusions are drawn in Section 5.

2. Computational setup

The three-dimensional, cylindrical release gravity currents in a stratified ambient have been simulated using Nek5000, a spectral element, incompressible flow solver (Fischer et al., 2008) with the Boussinesq approximation used to approximate the effects of gravity. It is hence assume that the density difference between two fluids is less than 5% (Turner, 1979) to neglect the influence of density differences in the inertia and diffusion terms and retain only in the buoyancy term (Cao et al., 2022, 2024). The nondimensional governing equations employed in the study take the form

$$\frac{\partial u_k}{\partial x_k} = 0,$$ (1)

$$\frac{\partial u_i}{\partial t} + u_k \frac{\partial u_i}{\partial x_k} = \rho e_i^g - \frac{\partial p}{\partial x_i} + \frac{1}{Re} \frac{\partial^2 u_i}{\partial x_k \partial x_k},$$ (2)

$$\frac{\partial \rho}{\partial t} + u_k \frac{\partial \rho}{\partial x_k} = \frac{1}{ReSc} \frac{\partial^2 \rho}{\partial x_k \partial x_k},$$ (3)

where ρ is the density of the fluid, u_i is the velocity for three-dimensional flow, p is pressure, and e_i^g is the unit vector in the direction of gravity. The dimensionless density, ρ is defined as

$$\rho = \frac{\rho^* - \rho_0^*}{\rho_c^* - \rho_0^*}$$ (4)

where the symbols ρ^*, ρ_0^*, and ρ_c^* with asterisks are the dimensional density of the local, top of the domain and heavy fluid respectively. The tensor notation in Eqs. (1)–(3) utilises subscripts i and k, where i represents an unrepeated index (also called a free index) that can take on values $i = 1, 2, 3$, and k represents a repeated index (also known as a dummy index) that signifies a summation over $k = 1, 2, 3$. The value of ρ is bounded between 0 and 1 if $S < 1$. The Schmidt number is Sc = ν^*/κ^* (where ν^* is the kinematic viscosity and κ^* is the molecular diffusivity). Although saline liquid, which is typically used in experiments, has Sc = 700; it is found that when Sc is in the order of 1 or larger, there is a weak scaling with the dynamics of the gravity current that does not significantly affect the bulk flow results (Härtel et al., 2000; Necker et al., 2005; Cantero et al., 2007b; Bonometti and Balachandar, 2008; Dai, 2015). It is common practice to set the Schmidt number to unity in numerical simulations of gravity currents. Therefore, Sc = 1 is used in current simulations to ensure numerical stability.

The height of the domain H^* is taken as the length scale. The velocity scale, U^*, time scale, T^* and the Reynolds number, Re are defined as

$$U^* = \sqrt{g'H^*}, \quad T^* = \frac{H^*}{U^*}, \quad Re = \frac{U^*H^*}{\nu^*},$$ (5)

where $g' = g^*(\rho_c^* - \rho_0^*)/\rho_0^*$ is the reduced gravity and g^* is the gravitational acceleration acting in the negative z direction. In the ambient, the dimensionless density at the bottom is $\rho_b = (\rho_b^* - \rho_0^*)/(\rho_c^* - \rho_0^*) = S$ where ρ_b^* is the density at the bottom of the ambient and S is the magnitude of the stratification. The dimensionless density in the

ambient ρ_a varies linearly with wall-normal height z from $\rho_a = \rho_b = S$ (where $\rho_a = (\rho_a^* - \rho_0^*)/(\rho_c^* - \rho_0^*)$ and ρ_a^* is density in the ambient) at the bottom ($z = 0$) to $\rho_a = \rho_0 = 0$ at the top ($z = 1$) and

$$\rho_a(z) = S(1 - z), \quad S = \frac{\rho_b^* - \rho_0^*}{\rho_c^* - \rho_0^*}.$$ (6)

Fig. 1 shows the initial configuration of full-depth cylindrical release gravity currents in a linearly stratified ambient with $S = 0.5$. The streamwise, spanwise and wall-normal directions are represented by x, y and z, respectively. The computational domain is a square prism with $L_x = L_y = 30$. At time $t = 0$, a cylindrical lock with a density of ρ_c^* has a height H^* and radius r_0^* is placed at the centre of the computational domain. Note that $r_0^* = H^*$ for all of the cases considered in this paper. The density of the ambient (ρ_a^*) is increased linearly from the top (ρ_0^*) to the bottom (ρ_b^*). A no-slip boundary condition is employed at the bottom ($z = 0$) of the domain and a slip, impermeable symmetry boundary condition is applied at the top of the domain ($z = H$) and vertical side walls ($x = [-L_x/2, L_x/2]$ and $y = [-L_y/2, L_y/2]$). The zero wall-normal gradient is set for all boundaries for the density field.

In this study, we have systematically investigated the effects of the stratification strength on the mixing of a cylindrical gravity current in a stratified ambient. Four stratification strengths of $S = 0, 0.2, 0.5,$ and 0.8 are considered and simulated at a moderate Reynolds number of Re = 3450. The number of spectral elements employed for the simulations at moderate Reynolds number Re are $N_x \times N_y \times N_z = 190 \times 190 \times 15$. The grid distribution within the spectral element follows the Gauss–Legendre–Lobatto (GLL) grid spacing. A 7th-order polynomial order is used in this study and the total number of unique grid points is approximately 1.9×10^8 grid points. Grid stretching (geometrical progression with power coefficient of 1.05) is applied along the wall-normal direction (z) where the grid size at the bottom part is denser than at the top. The computational grid has a grid spacing of $0.0033 \leqslant \Delta x = \Delta y \leqslant 0.0332$. The grid spacing to Kolmogorov scale ratio, $\Delta l/\eta$ (where $\Delta l = (\Delta x \Delta y \Delta z)^{1/3}$ and η is the Kolmogorov microscale) is calculated at different instantaneous time and is always less than 10. This is more conservative that than the $\Delta l/\eta \approx 16$ recommended by Zahtila et al. (2023) who studied the grid convergence characteristics of spectral element solvers. Therefore, we have ensured that our grid resolution is sufficient to resolve all of the turbulent length scales and also meet the requirement of $\Delta x = \Delta y \approx (ReSc)^{-1/2}$ where Sc = 1, see Härtel et al. (2000), Birman et al. (2005) and Dai (2015). A variable time step is used to ensure that the Courant number is always less than 0.5.

3. Evolution of the energy systems

The energy budget framework proposed by Winters et al. (1995) is based on the distinction between the adiabatic processes which allow for alterations in the initial potential energy without involving heat or mass exchange, and diabatic processes (Ottolenghi et al., 2016). This method is not dependent on the distinction between the volume of the dense and ambient fluid and hence does not require defining any interface between the dense and ambient fluid. This method is developed to carry out analysis of irreversible mixing in stratified flow and was applied in previous studies (Patterson et al., 2006; Fragoso et al., 2013; Ottolenghi et al., 2017) and will be used here. The equation for the time derivative of the kinetic energy (K) can be obtained by multiplying the momentum Eq. (2) by u_i, and has the expression

$$\frac{D}{Dt}\left(\frac{1}{2}u_i u_i\right) = -\frac{\partial}{\partial x_i}(pu_i)$$
$$+ \frac{2}{Re}\frac{\partial}{\partial x_j}(s_{ij}u_i)$$
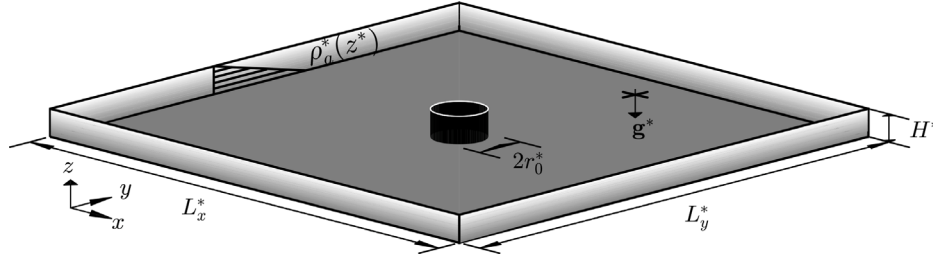$$- \frac{2}{Re}s_{ij}s_{ij} - g\rho u_3,$$ (7)

Fig. 1. Sketch of the computational domain for the three-dimensional simulation. The streamwise, spanwise and wall-normal directions are represented by x, y and z, respectively. The cylindrical region of heavy fluid located in the centre of the domain has a density of ρ_c^*. The heavy and ambient fluid has the same height as the height of the domain H^*. The density of the ambient $\rho_a^*(z^*)$ increases linearly from the top ρ_0^* to the bottom boundary ρ_b^* as indicated by the lighter grey shading and the $\rho_a^*(z^*)$ shown on the top left wall.

where D/Dt denotes the material or convective derivative, s_{ij} is the strain rate tensor where $s_{ij} = \frac{1}{2}(\partial u_i/\partial x_j + \partial u_j/\partial x_i)$ and u_3 is the velocity component in the z direction. The first two terms on the right-hand side of Eq. (7) are divergence terms, which vanish after integration over the flow domain Ω (Necker et al., 2005). Integration of Eq. (7) over the entire flow domain Ω provides the temporal evolution of the total kinetic energy K,

$$\dot{K} = \frac{dK}{dt} = -\frac{2}{Re}\int_\Omega s_{ij}s_{ij}dV - g\int_\Omega \rho u_3 dV, \tag{8}$$

$$K(t) = \frac{1}{2}\int_\Omega u_i u_i dV. \tag{9}$$

The potential energy in the system is defined as,

$$P(t) = g\int_\Omega \rho z dV. \tag{10}$$

We consider the changes in potential energy of the gravity current flow in a closed system and the time derivative of the potential energy can be determined using Eqs. (3) and (10) (Winters et al., 1995; Ng et al., 2016)

$$\dot{P} = \frac{dP}{dt} = \Phi_z + \Phi_i,$$
$$\Phi_z = g\int_\Omega \rho u_3 dV,$$
$$\Phi_i = -\kappa g A(\Delta\bar{\rho}), \tag{11}$$

where Φ_z represents the reversible rate of exchange with potential energy due to vertical buoyancy flux ($K \leftrightarrows P$), Φ_i represents a conversion of internal energy to background potential energy due to irreversible diffusion in the density field (Winters et al., 1995; Dai et al., 2021), $\Delta\bar{\rho}$ is the spatial averaging of the density difference between top ($\bar{\rho}(z = h_0, t)$) and bottom ($\bar{\rho}(z = 0, t)$) over the xz-plane and h_0 is the initial height of the heavy fluid.

The first term on the right-hand side of Eq. (8) represents the local rate of dissipation ϵ and the time integral of dissipation E_d has an expression

$$E_d(t) = \int_0^t \epsilon(\tau)d\tau, \quad \epsilon = \frac{2}{Re}\int_\Omega s_{ij}s_{ij}dV. \tag{12}$$

The summation of Eqs. (8) and (11) gives the change of total mechanical energy with time, $\dot{K} + \dot{P} - \Phi_i = \epsilon$. In the study by Birman et al. (2005), Φ_i is neglected (this will be discussed further below) and integrating it with respect to time yields $K + P + E_d = \text{const.} = K_0 + P_0$ (where K_0 is the initial kinetic energy and P_0 is the initial potential energy). This essentially represents an energy balance statement during the propagation of the gravity current.

3.1. Partitioning the potential energy and the instantaneous irreversible mixing

The potential energy of the system can be decomposed into background potential energy P_b and available potential energy P_a. According to Winters et al. (1995), changes in the potential energy of

the background state P_b are direct measure of the energy expended in mixing the fluid. In this context, the constant-density volumes are rearranged, with lighter volumes placed on top of the heavier volumes. The density field undergoes adiabatic rearrangement where the density of the fluid, ρ, increases from the top to the bottom of the domain. This results in redistributed fluid particles within the domain forming a perfectly stable horizontally stratified configuration (Winters et al., 1995; Ottolenghi et al., 2017) (see Fig. 2.) Adiabatic processes can modify the potential energy but they do not alter the background state $\bar{\rho}$. Only diabatic mixing can induce changes in the background state in closed systems. The background potential energy is the minimum potential energy attainable through an adiabatic redistribution of ρ and is defined as

$$P_b(t) = g\int_\Omega \rho\tilde{z}dV, \tag{13}$$

where $\tilde{z}$ is the vertical position in the reference state of the fluid parcel at position $(\boldsymbol{x}, t)$. The changes in the background potential energy are direct measures of the irreversible diapycnal mixing in the system which will be used to quantify the mixing efficiency in the system. The difference between the potential energy and the background potential energy, namely, the available potential energy, is expressed as

$$P_a(t) = g\int_\Omega \rho(z - \tilde{z})dV = P(t) - P_b(t). \tag{14}$$

The available potential energy is the potential energy released in an adiabatic transition from $\rho(z)$ to $\rho(\tilde{z})$ without altering the probability density function of density (Winters et al., 1995) and is the fraction of potential energy that can be converted to kinetic energy.

The mechanical energy exchange framework is summarised in Fig. 3. In our study, the system is configured as a closed system, and the diffusive transfers of heat and mass across the bounding surface are zero. Following Winters et al. (1995), the rate of change background potential energy and is expressed as

$$\dot{P}_b = \frac{dP_b}{dt} = -\kappa g\int_\Omega \frac{d\tilde{z}}{d\rho}|\nabla\rho|^2 dV = \Phi_d. \tag{15}$$

Since $P_a = P - P_b$, the rate of change of the available potential energy can be written as

$$\dot{P}_a = \frac{dP_a}{dt} = \Phi_z - (\Phi_d - \Phi_i). \tag{16}$$

Peltier and Caulfield (2003) illustrated that dP_b/dt is influenced by two physical processes, leading to irreversible changes in the density field (Agrawal et al., 2021). The rate of conversion of the internal energy to the potential energy, Φ_i, known as a microscopic process, would increase in the absence of macroscopic fluid motion. The other is the rate of mixing that are directly associated with macroscopic fluid motions. Peltier and Caulfield (2003) refer the terms on the right-hand side of Eq. (15) as $\mathcal{M} + \Phi_i$. The irreversible mixing rate, $\mathcal{M} = \Phi_d - \Phi_i$ can be written as

$$\mathcal{M} = \kappa g\left(-\int_\Omega \frac{d\tilde{z}}{d\rho}|\nabla\rho|^2 dV - A(\bar{\rho}_0 - \bar{\rho}_b)\right). \tag{17}$$
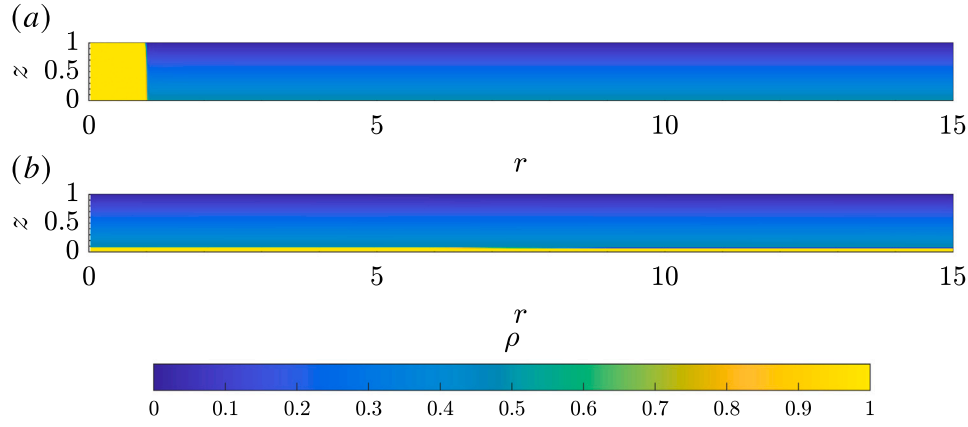
Fig. 2. 2D contour of the density field for the case with $S = 0.5$ in (a) original state and (b) rearranged density field with minimum potential energy state. The heavy fluid is coloured yellow and the density of the ambient $\rho_a(z)$ increases linearly from the top ρ_0 to the bottom boundary ρ_b as indicated by the blue shading. (For interpretation of the references to colour in this figure legend, the reader is referred to the web version of this article.)

It is important to emphasise that for flows with high Reynolds number, Φ_i is orders of magnitude smaller than Φ_d and can be disregarded in turbulent flows. However, in this study with a moderate Reynolds number of $Re = 3450$, Φ_i not negligible. The instantaneous mixing efficiency of the system, that is, the ratio of the rate of irreversible increase of background potential energy due to mixing $\mathcal{M}$ to the rate of the irreversible kinetic energy dissipation is then defined as

$$\eta_{m,i} = \frac{\mathcal{M}}{\mathcal{M} + \epsilon}. \tag{18}$$

where the numerator represents the irreversible mixing rate due to diapycnal mixing or the portion of the turbulent kinetic energy that is converted into useful work, while the denominator represents the irreversible losses of kinetic energy owning to both irreversible mixing and viscous dissipation (Peltier and Caulfield, 2003; Ilıcak, 2014; Mukherjee and Balasubramanian, 2021). Consequently, the cumulative mixing efficiency is given by

$$\eta_{m,c} = \frac{\int_0^t \mathcal{M}(\tau) d\tau}{\int_0^t \mathcal{M}(\tau) d\tau + \int_0^t \epsilon(\tau) d\tau}. \tag{19}$$

The definition of mixing efficiencies considers only the contribution of irreversibility and is not affected by the countergradient fluxes observed in strongly stratified flow (Venayagamoorthy and Koseff, 2016; Gregg et al., 2018).

4. Results and discussion

4.1. Energy budgets

Analysing the energy budget of the cylindrical current in both unstratified and stratified ambient conditions demonstrates the conversion process from available potential energy to kinetic energy and subsequent dissipation due to viscous friction. A comparison is made between the unstratified case and the stratified cases with $S = 0.2, 0.5$ and 0.8 to assess the effect of stratification on the energy exchange of the cylindrical release gravity current.

Fig. 4 shows the front velocity, u_f with varying S and non-dimensional potential energy budget of the gravity current propagating in the unstratified ambient $S = 0$ at $Re = 3450$. The transition of the gravity current for $S = 0$ case into different phases is plotted on Fig. 4(a). The evolution of the potential energies is illustrated in Fig. 4(b) and The corresponding reversible buoyancy flux (Φ_z), irreversible conversion of internal to potential energy (Φ_i) and time derivative of P_b (Φ_d) is shown in Fig. 4(c). At $t = 0$, when the fluid is stationary with no kinetic energy, the total energy is stored as potential energy. The non-dimensional available potential energy,
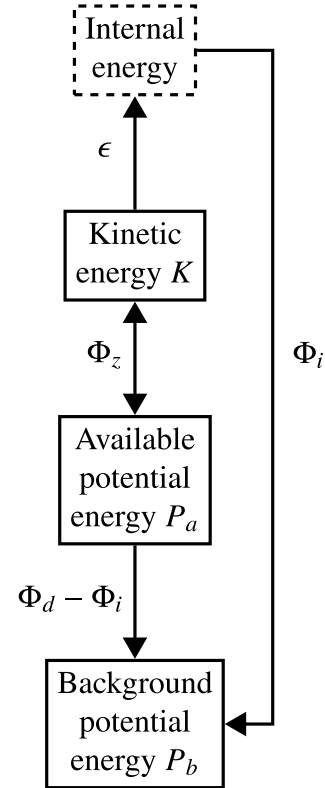

Fig. 3. Mechanical energy framework (Winters et al., 1995) for gravity current flow in a stratified environment. The arrows shows the pathways for the energy conversion between P_b the background potential energy, P_a the available potential energy and K the kinetic energy. The irreversible kinetic energy dissipation is ϵ, Φ_z is the reversible buoyancy flux, Φ_d is the irreversible diapycnal mixing and Φ_i is the irreversible conversion of internal to background potential energy.

P_a, is approximately 1, indicating that the potential energy is totally imputable to the conversion to kinetic energy (Ottolenghi et al., 2016). The non-dimensional background potential energy in Fig. 4(b) is small but not zero, and it is the same for Φ_d. Since there is no fluid motion, Φ_z equal to zero. The irreversible conversion of internal to potential energy, Φ_i, is also zero because there is no difference between the mean densities at the top and bottom boundary.

During the initial acceleration phase ($0 < t \leqslant 2.5$) after the heavy fluid is released into the ambient fluid, both P and P_a decrease rapidly, reaching nearly the same values. Background potential energy, P_b,
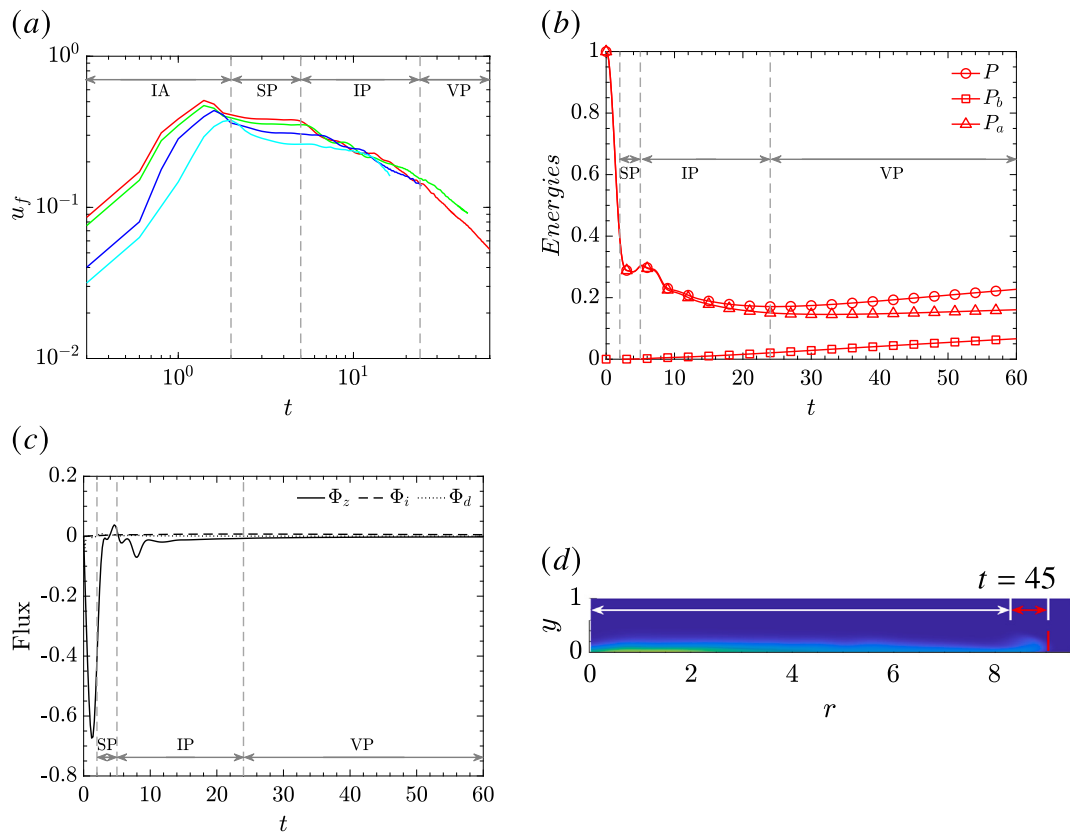
Fig. 4. The plot of (*a*) front velocity against time with different S, (*b*) non-dimensional potential energies and (*c*) evolution of Φ_z(——), Φ_i(– – –) and Φ_d(– · – ·) as a function of time for $S = 0$. 2D azimuthal-averaged density contour at $t = 45$ is shown in (*d*). The colour of the contour is saturated and is six times smaller than the original. The red and white arrows indicate the head and tail of the gravity current. Total potential energy P, (○); background potential energy P_b, (□) and available potential energy P_a, (△). The colour in (*a*) represents different S, ——, $S = 0$; ——, $S = 0.2$; ——, $S = 0.5$ and —— and $S = 0.8$. The transition of the current label in (*a*) is for $S = 0$ case, IA: initial acceleration and deceleration; SP: slumping phase; IP: inertial phase and VP: viscous phase. (For interpretation of the references to colour in this figure legend, the reader is referred to the web version of this article.)

remains close to zero, demonstrating the conversion from potential energy to kinetic energy. In this phase, Φ_z is negative and dominant compared to Φ_d and Φ_i due to the drop of potential energy.

As the current transitions into the slumping phase ($2 < t < 5$), the speed of the current reaches near-constant (refer to Fig. 4(*a*)) and Kelvin–Helmholtz billows form behind the current head. During this phase, P and P_a show slight increase from a trough, resulting in Φ_z increasing and becoming positive. This indicates reversible stirring of the heavy fluid into the body of the current and irreversible mixing with the ambient fluid caused by Kelvin–Helmholtz billows (Ottolenghi et al., 2016) (see Fig. 5(*b*) and (*c*)), making Φ_d greater than Φ_i. Although the value of P_b is low, the increase in P_b reflects the presence of non-zero irreversible mixing, where the trapping of ambient fluid due to Kelvin–Helmholtz billows alters the potential energy and slightly changes the background potential energy (Ottolenghi et al., 2016).

As the current transitions into the self-similar inertial phase, P and P_a continue to decrease until approximately $t \approx 24$, while P_b continues to increase as the current propagates. During this phase, P_a gradually separates from the curve of P, which shows the variation of P is caused more by the irreversible mixing of fluid elements than reversible stirring ($P_a \rightarrow K$). The buoyancy flux remains negative throughout the propagation of the current, indicating that potential energy monotonically decreases (Dai et al., 2021).

At later times ($t > 24$), the current enters the self-similar viscous phase where the viscous force dominates the buoyancy force, resulting in a rapid decay of the current's speed. Both P and P_a begin to increase, with P growing at a higher rate until the end of the simulation. During the viscous phase, the increase P is mainly attributed to laminar diffusive processes rather than the transfer from kinetic energy to available potential energy. This observation suggests that the density difference between the heavy fluid and ambient fluid becomes smaller, leading to increased mixing within the current.

Finally, when $t > 40$, the propagation of the current becomes negligible as there is insufficient density difference between the current and ambient at the bottom wall to continue propagating. The increase in available potential energy, P_a, may be attributed to the presence of fluid with greater density than the ambient density remaining almost stationary within the tail of the gravity current. Similarly, Φ_z increases due to the rise in potential energy. As reported by Peltier and Caulfield (2003), Φ_i is the rate at which potential energy of a statistically stable density distribution would increase in the absence of macroscopic fluid motion. In the self-similar phase, fluid is hardly moving at the tail of the gravity current. So the average density at the bottom is larger than the top. This should increase Φ_i and hence Φ_i will contribute to the increase in P. This can be visualised in Fig. 4(*d*) where fluid stagnant in the tail of the current ($0 \leqslant r < 4$) has density higher than the head. The head and tail of the gravity current are annotated by the red and white arrows.

The evolution of the gravity current propagating in both unstratified (left column) and stratified ambient with $S = 0.5$ (right column) are shown in Fig. 5. The red vertical lines indicate the front location of the current and white arrows represent the Kelvin–Helmholtz billows. At an early time, $t = 1$, the heavy fluid slumps into the ambient fluid, and both cases do not show a significant difference. During the slumping phase, between $3 < t < 5$, Kelvin–Helmholtz billows are observed forming behind the current head for the unstratified case at $t = 3$. For $S = 0.5$, the Kelvin–Helmholtz billows form at $t = 5$. At this time ($t = 5$), the current in the unstratified case travels significantly greater distance
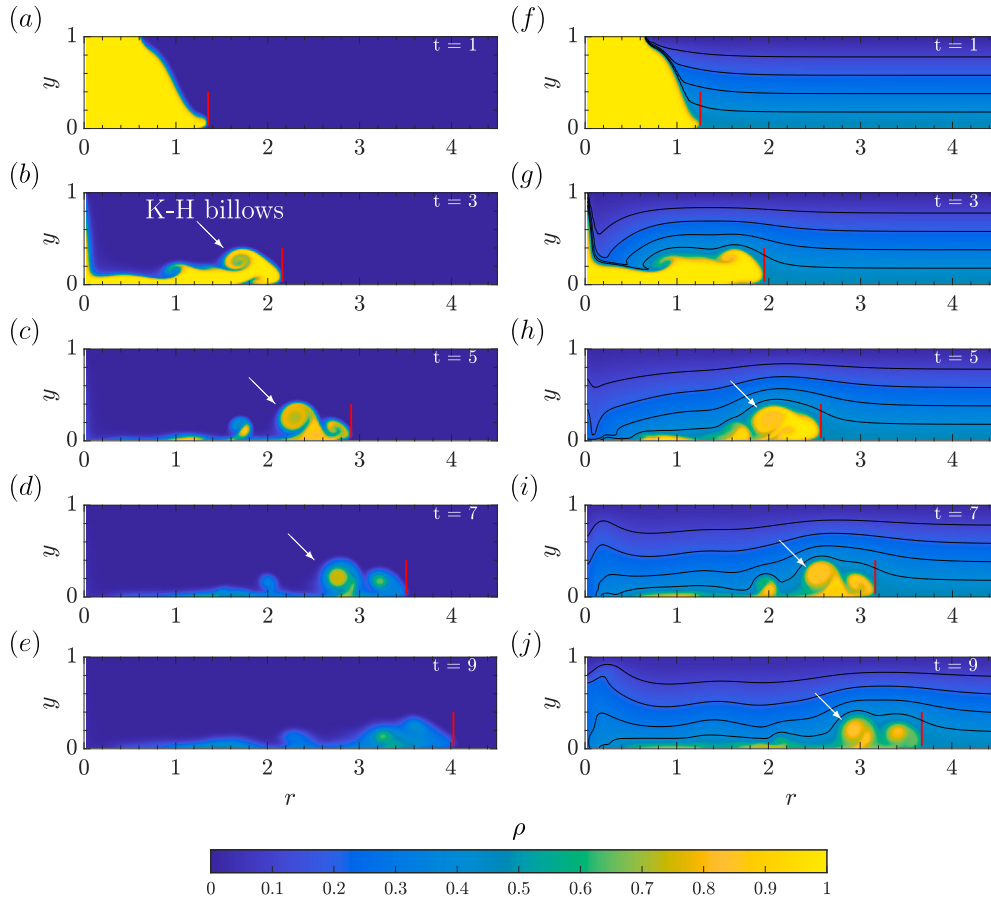
Fig. 5. Time evolution of the azimuthal-averaged gravity current in the stratified ambient with $S = 0$ (left column) and 0.5 (right column). Contours are shown with time intervals of 2 time units. The heavy fluid is coloured yellow and the density of the ambient $\rho_a(z)$ increases linearly from the top ρ_0 to the bottom boundary ρ_b as indicated by the blue shading. The solid black line represents the isopycnals. The red vertical lines indicate the front position of the gravity current. The white arrows represent the Kelvin–Helmholtz billows behind the gravity current head. (For interpretation of the references to colour in this figure legend, the reader is referred to the web version of this article.)

than in $S = 0.5$. At this time ($t = 5$), the current in the unstratified case travels a significantly greater distance than in $S = 0.5$. This indicates that stratification hinders the propagation of the gravity current, delays the vortex formation, and results in less turbulence (Dai et al., 2021; Lam et al., 2024).

Interestingly, at $t = 7$ and $t = 9$ where the current is in the inertial phase, the current with $S = 0.5$ exhibits a similar contour compared to the unstratified case at $t = 5$ and $t = 7$, indicating that the development of the Kelvin–Helmholtz billows is delayed by approximately 2 time units. At $t = 9$, the merging of the K–H billows with the head of the gravity current is observed for the unstratified case. However, for $S = 0.5$, the K–H billows do not merge with the head (not shown here) but begin to separate from it. This occurs because the gravity current transitions into subcritical flow, where the internal gravity waves separate from the current head, move upstream and faster than the current, and break down the merging of the billows with the head (Maxworthy et al., 2002; Lam et al., 2024). These figures illustrate the contribution of the Kelvin–Helmholtz billows on the evolution of the available potential energy P_a and the background potential energy P_b.

The normalisation for the potential energy is given by,

$$P = (P^* - P_b^*(0))/P_a^*(0)$$
$$P_b = (P_b^* - P_b^*(0))/P_a^*(0)$$
$$P_a = P - P_b, \tag{20}$$

where the P^*, P_b* and P_a^* are the dimensional total potential energy, background potential energy and available potential energy. The initial

available potential energy, $P_a^*(0)$ is the potential energy that is available to be converted to kinetic energy. The total potential energy, P and background potential energy, P_b are normalised with respect to the initial available potential energy $P_a^*(0)$.

The dimensional (left column) and non-dimensional (right column) potential energy budget with different S at Re $= 3450$ are shown as in Fig. 6. The background potential energy at $t = 0$ ($P_b^*(0)$) is subtracted from P^* and P_b^*. At the beginning of the simulation, the initial dimensional potential energy is approximately 4502 kg m^2/s^2, as shown in Fig. 6(a). The corresponding dimensional total potential energy is 4532 kg m^2/s^2 for $S = 0.2$, 4576 kg m^2/s^2 for $S = 0.5$ and 4612 kg m^2/s^2 for $S = 0.8$. The increase in P at $t = 0$ with increasing S due to the increasing background potential energy attributed to stratification in the ambient (see Fig. 6(c, d)). Specifically, the dimensional available potential energy at $t = 0$ ($P_a^*(0)$) is lower for a higher value of S, as illustrated in Fig. 6(e). The non-dimensional total potential energy for different S increases rapidly at $t > 5$ due to the oscillation of internal gravity wave behind and above the gravity current. After the release of the heavy fluid, it slumps into the ambient fluid, forming the gravity current. As a result, the fluid parcel in the ambient undergoes an upward and backward shift from its equilibrium position. This process is illustrated in Fig. 7 for the range $2.8 < r < 3.6$. Within the range $0 < r < 1$, the stratified ambient arrangement behind the gravity current is in a non-equilibrium state (due to the oscillation of the internal gravity waves) and deviates from its initial linearly stratified arrangement. Similarly, the arrangement of the fluid parcel above the gravity current head, as well as above the Kelvin–Helmholtz billows, is higher than its original position, resulting in an
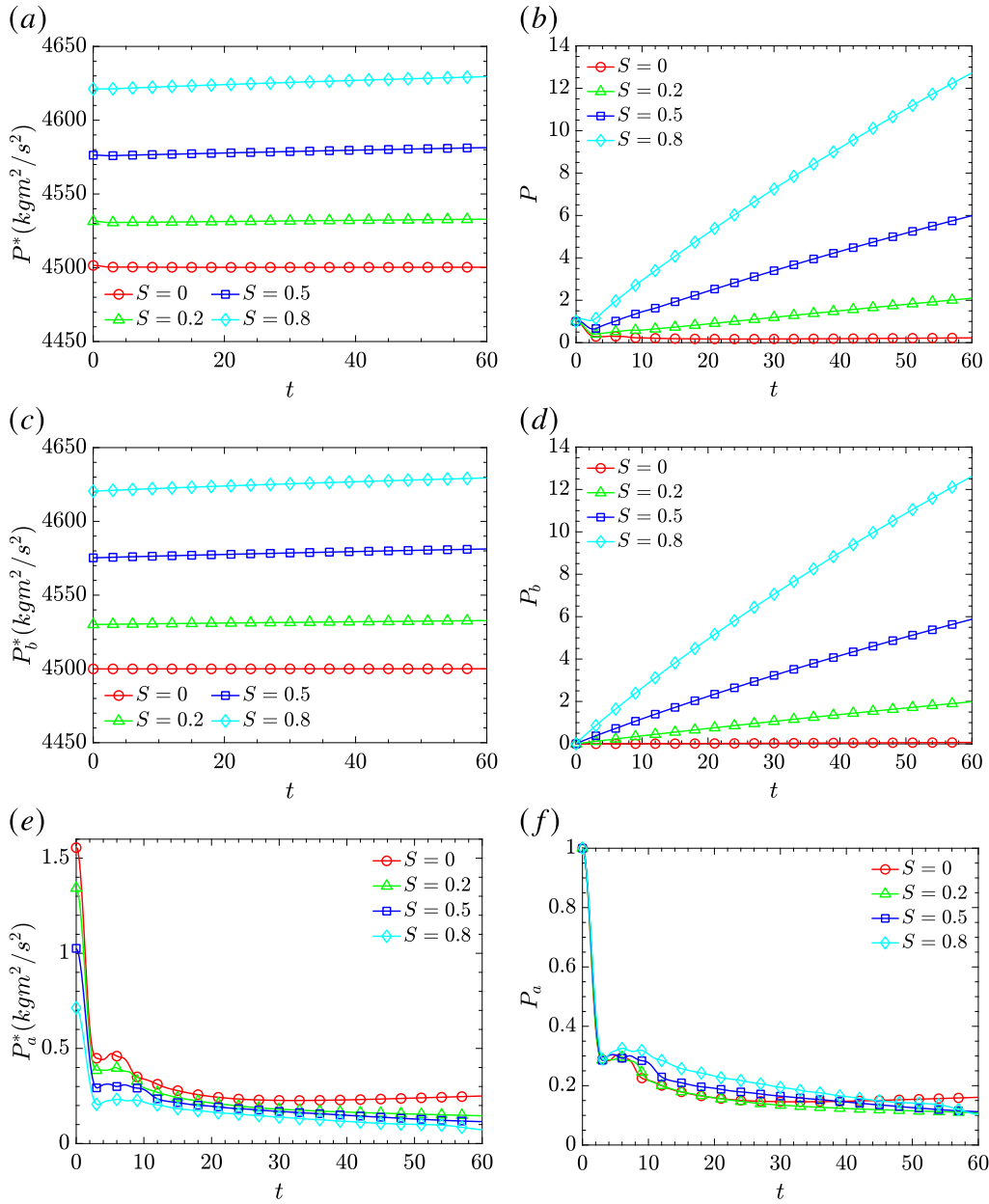
Fig. 6. Dimensional (a, c, e) and non-dimensional (b, d, f) potential energies as a function of time with S varying from 0 to 0.8 at $\mathrm{Re} = 3450$. Total potential energy P, ($\circ$); background potential energy P_b, ($\square$); and available potential energy P_a, ($\triangle$). The energies on the tight column are normalised with initial available potential energy. The colour represents different S, —, $S = 0$; —, $S = 0.2$; —, $S = 0.5$ and — and $S = 0.8$. (For interpretation of the references to colour in this figure legend, the reader is referred to the web version of this article.)

increase in potential energy. This can be visualised in Fig. $5(g)-(j)$ for $S = 0.5$. The density field then adiabatically rearranges into a state of minimum potential energy. As the density in the ambient is non-zero $(t > 0)$, P_b also increases. Total potential energy, P and background potential energy, P_b continue to increase until the end of the simulation for stratified cases and have a higher value with increasing S. The increase in P_b is attributed to diffusive mixing, as stated by Winters et al. (1995). Background potential energy, P_b of stratified cases as shown in Fig. $6(c, d)$ is significantly greater than in the unstratified case, suggesting that the variation in P for stratified cases is mainly due to the irreversible mixing of the ambient fluid rather than the reversible stirring of the heavy fluid within the current.

The plot of the dimensional and non-dimensional available potential energy for different S in Fig. $6(e, f)$ show a similar trend with the unstratified case until approximately $t \approx 24$. However, in the stratified cases, P_a continues to decrease throughout the simulation. This trend

occurs because the propagation of the current becomes negligible in the stratified cases, primarily due to an insufficient density difference between the current and ambient fluid at the bottom wall. Consequently, the fluid on the bottom wall, with a density closest to the bottom boundary, remains stationary and continues to mix with the ambient fluid. This scenario leads to minimal, if any, conversion between available potential energy and kinetic energy within the gravity current. The increase in background potential energy further highlights the consequences of irreversible diapycnal mixing.

Fig. $8(a)$ and (b) show the temporal evolution of kinetic energy, K and buoyancy flux, Φ_z as a function of time with S ranging from 0 to 0.8 at $\mathrm{Re} = 3450$. In Fig. $8(c)$ and (d), the plots demonstrates the behaviour of the instantaneous dissipation, ϵ and cumulative dissipation, E_d over time for different S cases. Both kinetic energy and cumulative dissipation are normalised with respect to initial available potential energy $P_a(0)$, the sole source of energy available for the stirring process.
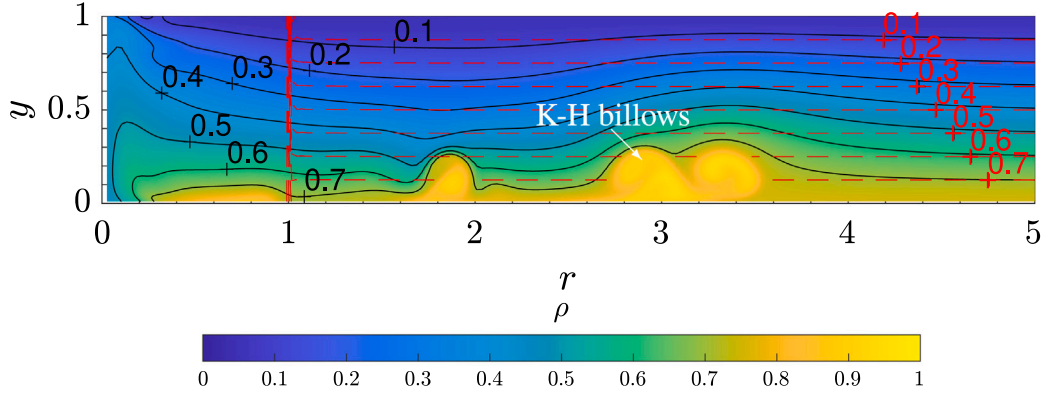
Fig. 7. Azimuthal-averaged 2D density contour of gravity current propagating into a linearly stratified ambient with $S = 0.8$. The black solid lines in the ambient represents the isopycnals at $t \approx 10$ and the red dashed lines represent the initial condition of the simulation ($t = 0$). The black crosses on the left indicate the density level of the ambient at $t \approx 10$, which is in a non-equilibrium state. The red crosses represent the initial density level of the ambient in the linearly stratified arrangement at $t = 0$. (For interpretation of the references to colour in this figure legend, the reader is referred to the web version of this article.)
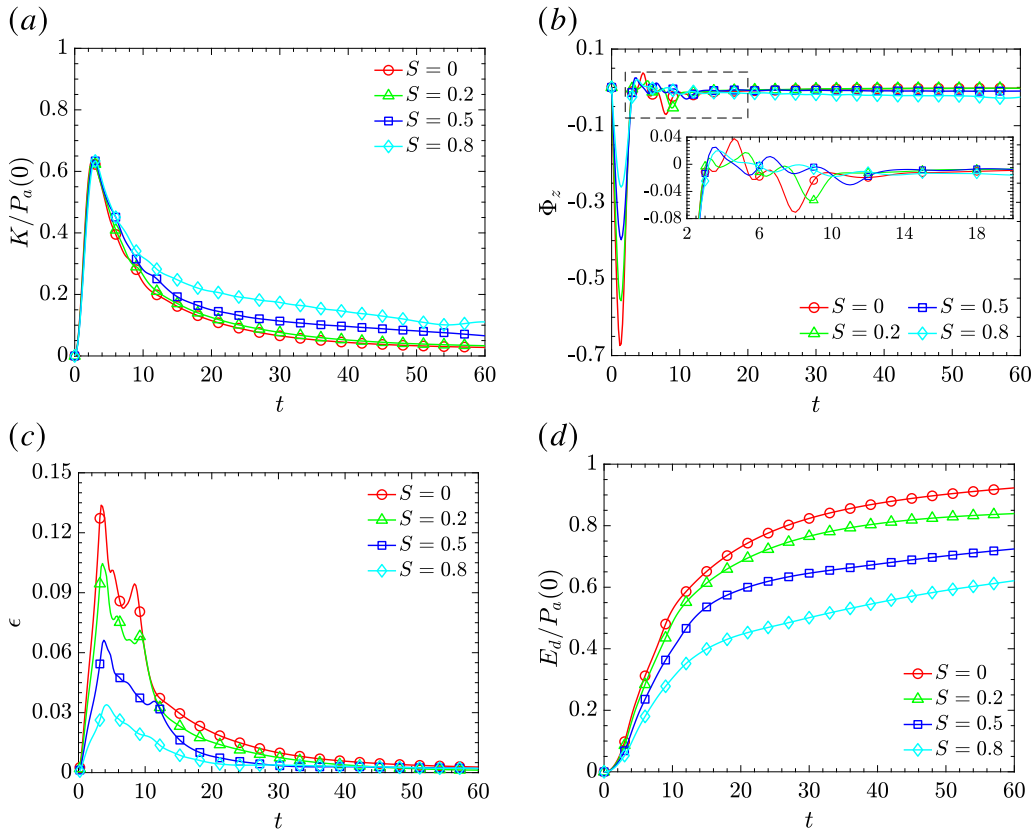

Fig. 8. Plot of (a) kinetic energy ($\diamond$), (b) reversible buoyancy flux Φ_z, (c) dissipation and (d) cumulative dissipation ($\times$) with S varying from 0 to 0.8 at Re = 3450. Kinetic energy and cumulative dissipation are normalised with initial available potential energy. The colour represent different stratification strength, ——, $S = 0$; ——, $S = 0.2$; ——, $S = 0.5$ and ——, $S = 0.8$. (For interpretation of the references to colour in this figure legend, the reader is referred to the web version of this article.)

As the heavy fluid is released and slumps into the ambient, kinetic energy rapidly increases due to its conversion from available potential energy. In Fig. 8(a), all cases exhibit a similar peak normalised kinetic energy of approximately $K/P_a(0) \approx 0.65$ between $2.6 < t < 3$. This indicates that up to about 65% of the initial available potential energy $P_a(0)$ is converted to kinetic energy regardless of the stratification strength of the ambient. Note that $P_a(0)$ increases with increments of S as observed in Fig. 6(e). Kinetic energy reaches its maximum and available potential energy (P_a) in Fig. 6(e, f) reaches a local minimum at the same time before the gravity current transitions into the slumping phase, characterised by the front velocity reaching an almost constant value. During the slumping phase, K decreases while both P_a and P_b

increase, which indicates irreversible mixing of fluid elements. The formation of Kelvin–Helmholtz billows contributes to reversible stirring of the dense fluid into the body of the current and permanent irreversible mixing with the ambient fluid. Subsequently, as the current transitions into the inertial phase, characterised by a power-law decay in the front velocity, kinetic energy decreases, resulting in a less energetic current.

The buoyancy flux, Φ_z of the gravity current at Re = 3450 with varying S is presented in Fig. 8(b). Soon after the heavy fluid is released, Φ_z decreases to a local minimum, indicating the conversion of available potential energy to kinetic energy. During the time $2 < t < 14$, the oscillation of Φ_z shows the reversible conversion between the potential energy and kinetic energy. Interestingly, the amplitude of the
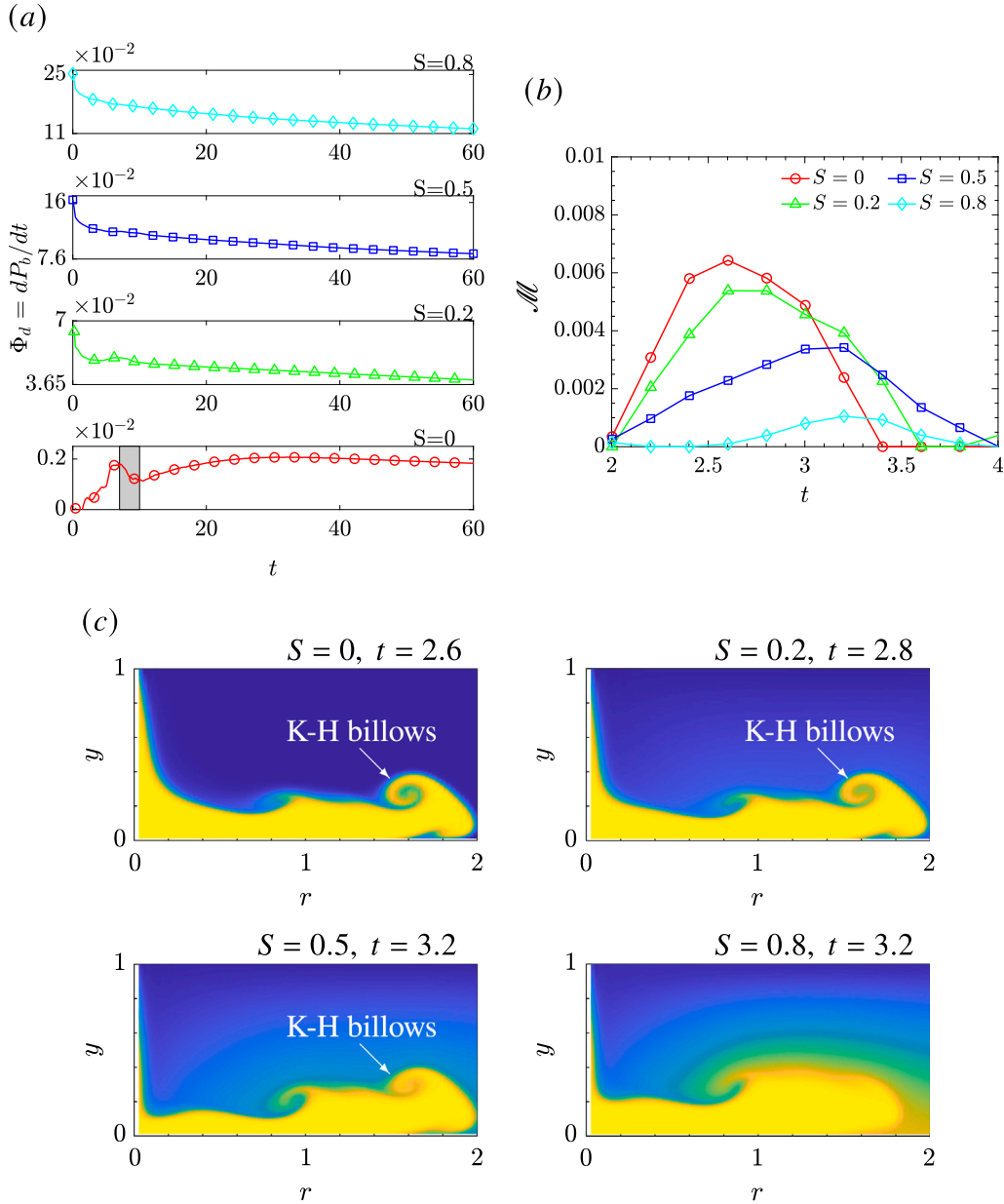
Fig. 9. Plot of the (*a*) time derivative of background potential energy, $dP_b/dt = \Phi_d$ (∗), (*b*) mixing rate during the slumping phase, $\mathcal{M} = \Phi_d - \Phi_i$ (——) against time with S and (*c*) azimuthal-averaged 2D density contour when $\mathcal{M}$ reaches its local maximum with S varying from 0 to 0.8 at Re = 3450. The grey region indicates the drop in Φ_d showed in Fig. 10. The colour represent different stratification strength, ——, $S = 0$; ——, $S = 0.2$; ——, $S = 0.5$ and ——, $S = 0.8$. (For interpretation of the references to colour in this figure legend, the reader is referred to the web version of this article.)

oscillation for the unstratified case is significantly greater than for the stratified cases, indicating a more energetic exchange. With increasing S, the amplitude of the oscillation decreases, resulting in lower energy exchange. At $t > 14$, Φ_z reaches almost constant and there is no (or minimal) conversion between K and P_a.

In general, both the kinetic energy and available potential energy in the system decrease with increasing S. This observation implies that the potential energy available for conversion into kinetic energy is influenced by the degree of stratification. Furthermore, the decrease in the amplitude of the oscillation in Φ_z with increasing S indicates a reduced rate of conversion from potential to kinetic energy. This finding aligns with the conclusions of Birman et al. (2005), who reported an increased rate of potential energy conversion with decreasing density ratio. In this study, the density ratio can be written as $\gamma_S = \rho_\alpha/\rho_c$ where $\rho_\alpha = (\rho_0 + \rho_b)/2$, and γ_S increases as S increases. On the other hand, Dai et al. (2021), who studied the propagation of planar currents

in a stratified ambient, reported that the stratification in the ambient can hinder the release of potential energy associated with the current, which aligns with the result of Φ_z in Fig. 8(*b*).

Fig. 8(*c*) presents the instantaneous dissipation of the gravity current in both unstratified and stratified environments at Re = 3450. In the unstratified case, the gravity current exhibits the highest peak kinetic energy compared to the stratified cases, indicating stronger turbulence and greater energy conversions. The increase in the kinetic energy reflects a higher velocity gradient and leads to an increase in the dissipation rate, ϵ. In a stratified environment, the presence of stratification leads to a decrease in the effective density difference between the heavy fluid and the ambient fluid, resulting in a reduced buoyancy force acting on the gravity current. As a result, the front velocity of the current decreases during the initial acceleration and slumping phases, leading to lower kinetic energy. This reduction in kinetic energy corresponds to a decrease in the dissipation rate. Gravity
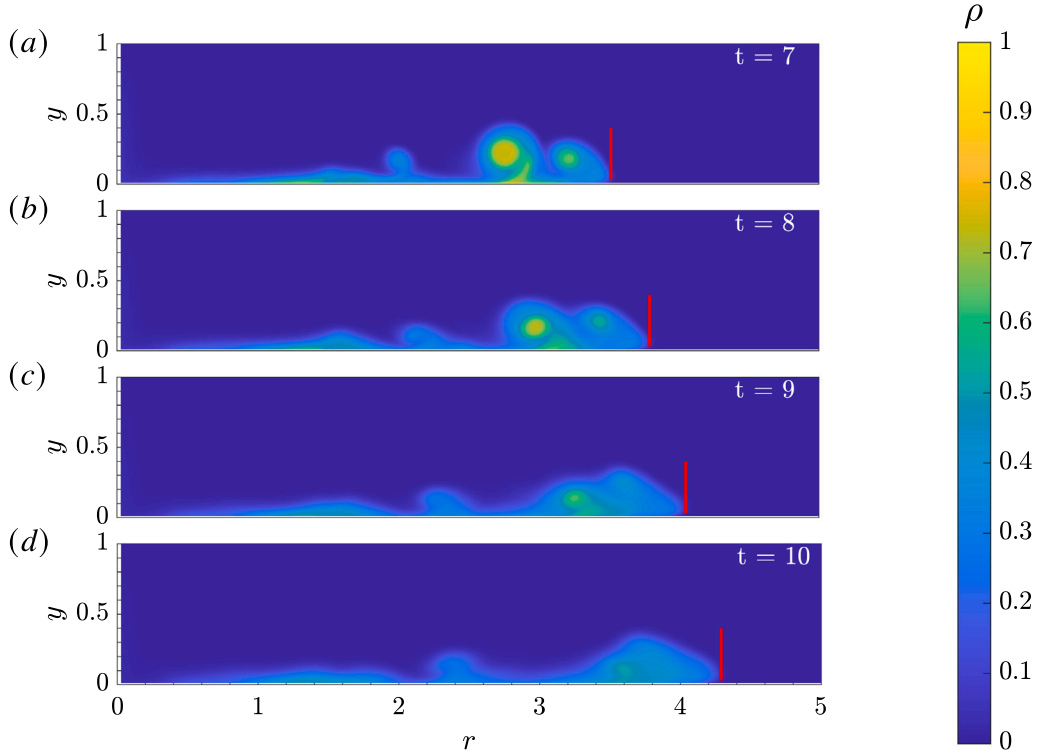
Fig. 10. Time evolution of the azimuthal-averaged gravity current in the unstratified ambient $S = 0$. Contours are shown with time intervals of 1 time unit. The heavy fluid is coloured yellow and the density of the ambient $\rho_a(z) = \rho_0$ is coloured blue. The red vertical lines indicate the front position of the gravity current. (For interpretation of the references to colour in this figure legend, the reader is referred to the web version of this article.)
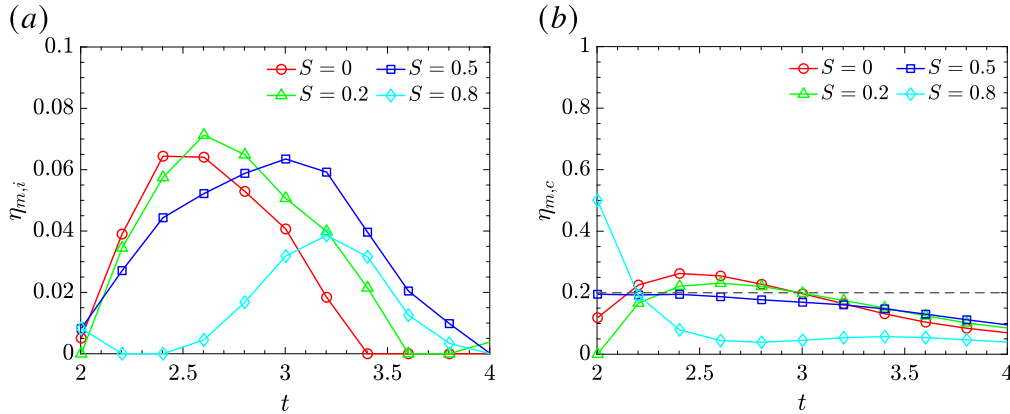

Fig. 11. Instantaneous $\eta_{m,i}$ (∗) and cumulative $\eta_{m,c}$ (∘) mixing efficiency as a function of time with S varying from 0 to 0.8 at Re = 3450. The dash-dotted line (−·−·) on (b) represented the characteristic of cumulative mixing efficiency $\eta_{m,c} = 0.2$ reported by Peltier and Caulfield (2003) catalysed by the development of Kelvin–Helmholtz instabilities. ——, $S = 0$; ——, $S = 0.2$; ——, $S = 0.5$ and ——, $S = 0.8$.

currents propagating into a linearly stratified ambient have a smaller density difference compared to those propagating into an unstratified ambient. Consequently, the buoyancy force acting on the current is lower, resulting in reduced energy dissipation.

When the gravity current transitions into the slumping phase and the front velocity becomes approximately constant, the dissipation rate initially decreases. However, in the cases of $S = 0, 0.2$ and 0.5, a significant increase in the dissipation rate is observed at $7 < t < 12$ due to the presence of the Kelvin–Helmholtz billows behind the current head (see Fig. 7). However, this increase is not significant for the $S = 0.8$ case. These billows cause reversible stirring of the heavy fluid into the body of the current leading to an increase in the dissipation rate. As the billows begins to merge with the current head, the dissipation rate starts to decrease again. The dissipation rate continues to decrease until

it reaches an approximately constant value close to zero. This occurs when there is insufficient density difference between the current and ambient at the bottom wall and the propagation of the current becomes very small for all cases.

Examining the plot of cumulative dissipation of kinetic energy against time in Fig. 8(d), it can be observed that E_d increases rapidly after the release of the heavy fluid until approximately $t \approx 20$, and then continues to increase at a slower rate in the later times in all cases. When the viscous forces dominate over buoyancy forces ($t \geqslant 20$) and the density difference between the heavy fluid and ambient fluid becomes smaller, the propagation of the current becomes negligible, leading to a decrease in the rate of increase in E_d.

Based on the above analysis, it can be concluded that the potential energy available for conversion to kinetic energy decreases with

increasing stratification strength in the ambient. This is reflected in the observation that the peak kinetic energy scales exactly with the initial available potential energy, $P_a^*(0)$. Consequently, gravity currents propagating in a stratified environment are less energetic compared to those in an unstratified environment. This finding is consistent with previous reports by Ungarish and Huppert (2006) and Dai et al. (2021).

4.2. Rate of irreversible mixing and mixing efficiency

In this section, the rate of irreversible mixing, $\mathcal{M}$ and mixing efficiency, η_m will be discussed. The focus will be on the mixing process of the cylindrical gravity currents with varying S during the slumping phase ($2 \leqslant t \leqslant 4$), coinciding with the period where the kinetic energy of the current reached a local maximum. Strong Kelvin–Helmholtz billows formed during the slumping phase contribute to both the reversible stirring of heavy fluid into the current and irreversible mixing with the ambient fluid (Ottolenghi et al., 2016). This scenario can be compared to studies on stratified shear flow (Winters et al., 1995; Peltier and Caulfield, 2003; Salehipour and Peltier, 2015), which employ a similar method to determine the mixing efficiency of mixing layers.

As the gravity current transitions into the self-similar phase, applying this method to evaluate mixing efficiency becomes challenging due to the nearly stagnant fluid within the long tail of the current, leading to the local values of Φ_i becoming greater than Φ_d in these regions. The influence of stratification on the rate of irreversible mixing process is examined by plotting the temporal derivative of background potential energy, $\dot{P}_b = \Phi_d$ and mixing rate, $\mathcal{M}$ of the gravity current in both unstratified and stratified environments at Re = 3450, as illustrated in Fig. 9. It is worth noting that the mixing rate, $\mathcal{M}$ of the gravity current with varying S is specifically plotted during the slumping phase.

Examining the temporal derivative of background potential energy in Fig. 9(a), in the $S = 0$ case, Φ_d initially experiences a steep rise until the end of the slumping phase around $t \approx 6$. Following this, it fluctuates around an approximately constant value until $t \approx 7$. Subsequently, the curve rapidly decays until around $t \approx 10$, after which it begins to increase again. The drop in Φ_d (grey region) is attributed to the merging of the Kelvin–Helmholtz billows with the current head, causing a reversible stirring of the heavy fluid into the current head as shown in Fig. 10. The increase of Φ_d occurs when the billows have fully merged with the head. Around $t \approx 30$, the curve reaches a local maximum of approximately 0.002, followed by a gradual decrease until the end of the simulation. The decrease of Φ_d at $t > 30$ coincides with the transition of the current into the viscous phase, where the turbulent structures break down and become more three-dimensional (Ottolenghi et al., 2016).

Interestingly, when stratification is present in the ambient environment, Φ_d exhibits a higher value at the beginning of the simulation, and it further increases with increasing stratification strength S. This behaviour can be attributed to the fact that the background potential energy increases as the stratification strength S increases, leading to a greater rate of change of P_b during the initial stages of the simulation. The evolution of Φ_d for stratified cases is different compared to the unstratified case. After the release of the heavy fluid into the ambient, Φ_d decreases for the stratified cases while it increases for the unstratified case (see the red plot in Fig. 9(a)). However, there is a slight increase in Φ_d for $S = 0.2$ during the time interval $4.4 < t < 6.5$ and for $S = 0.5$ during the interval $6.2 < t < 7.2$. This increase is attributed to the separation of the Kelvin–Helmholtz billows from the current head, as they become part of the current body (see Fig. 5(j) for the case with $S = 0.5$). For $S = 0.8$, Φ_d exhibits a continuous decrease from the beginning to the end of the simulation.

The mixing rate, $\mathcal{M}$, of the cylindrical gravity current during the slumping phase at Re = 3450 is illustrated in Fig. 9(b) for varying S cases. The peaks of mixing rate for $S = 0, 0.2, 0.5$, and 0.8 are $0.0064, 0.0054, 0.0034$, and 0.0011 respectively. It is evident that the

mixing rate of the gravity current decreases with increasing stratification strength, and the time for the gravity current to reach the peak mixing rate increases with higher stratification strength. Fig. 9(c) shows the 2D density contour of the azimuthal-averaged gravity current when the mixing rate reached local maximum during the slumping phase. Kelvin–Helmholtz billows form behind the head, transporting the heavy fluid towards the head and mixing it irreversibly with the ambient fluid. The decrease in the mixing rate is attributed to the reduction in the size of the Kelvin–Helmholtz billows behind the head with increasing stratification, indicating a less energetic reversible stirring process. For the $S = 0.8$ case, no Kelvin–Helmholtz billows are observed behind the head, resulting in a less turbulent gravity current and a lower mixing rate compared to the other cases.

We will focus on the mixing process during the slumping phase and compute both the instantaneous and cumulative mixing efficiency as

$$\eta_{m,i} = \frac{\mathcal{M}(t_{SP})}{\mathcal{M}(t_{SP}) + \epsilon(t_{SP})}$$
$$\eta_{m,c} = \frac{\int_{t_{SP}} \mathcal{M}(\tau)d\tau}{\int_{t_{SP}} \mathcal{M}(\tau)d\tau + \int_{t_{SP}} \epsilon(\tau)d\tau} , \qquad (21)$$

where $t_{SP} \in [4, 6]$. Fig. 11 illustrates the temporal evolution of the instantaneous ($\eta_{m,i}$) and cumulative ($\eta_{m,c}$) mixing efficiency for varying stratification strength (S) cases at Re = 3450 during the slumping phase. Soon after the lock is released, the heavy fluid slumps and undergoes initial acceleration. The instantaneous mixing efficiency is close to zero for all cases, indicating minimal mixing during this early phase. Notably, at $t = 2$, in the stratified case, $\eta_{m,i}$ is slightly greater than in the unstratified case due to larger Φ_d (see Fig. 9(a)) with increasing S. Similarly, $\eta_{m,c}$ at $t = 2$ for stratified cases is higher than in the unstratified case are attributed to the higher Φ_d and low cumulative dissipation as shown in Fig. 8(d).

Reviewing both the instantaneous and cumulative mixing efficiencies, a faster increase in mixing efficient is observed for the unstratified case, coupled with a decrease with increasing stratification. Interestingly, cases with $S = 0, 0.2$ and 0.5 exhibit a similar peak of $\eta_{m,i}$, corresponding to the development of Kelvin–Helmholtz billows behind the head (see Fig. 9(c)). In the strongly stratified case ($S = 0.8$), $\eta_{m,i}$ is significantly lower compared to the other cases due to less turbulence in the gravity current. Notably, Peltier and Caulfield (2003) reported a characteristic mixing efficiency of the order of 0.2 resulting from the development of Kelvin–Helmholtz instabilities, and this is plotted in Fig. 11(b) for comparison with the present study. For the cases with $S = 0, 0.2$, and 0.5, $\eta_{m,c}$ shows a fair agreement with the values reported by Peltier and Caulfield (2003) at $t < 3.5$, but the strongly stratified case exhibits $\eta_{m,c}$ that is significantly lower than the reported value.

In the study by Mukherjee and Balasubramanian (2021), cumulative mixing efficiency of approximately $0.12 - 0.14$ is reported for $Re \geq 3000$. This low mixing efficiency is attributed to a large Prandtl number, Pr, as salt in water diffuses much slower compared to thermally stratified air (note that $Pr = 1$ in the present study). Additionally, they reported that mixing efficiency can increase in strongly stratified flow with a sufficiently large turbulent Reynolds number, $Re_T = (T_L/T_\eta)^2$ (where T_L is the time needed for turbulent kinetic energy to cascade from the largest to the smallest scales, and T_η is the timescale at which viscous dissipation occurs or is loosely equivalent to the timescale at which eddy diffusion occurs), which could sustain turbulence and mixing.

During the slumping phase, the front velocity of the current remains relatively steady. We computed the local Reynolds number, $Re_L = u_{f,mean}(t_{SP})H/\nu$ for each case. The local Reynolds number for $S = 0, 0.2, 0.5$ and 0.8 are 1326, 1228, 1071 and 903, respectively. For the case with $S = 0.0(0.8)$, Re_L is approximately 2.5(3.8) times smaller compared to Re fixed in the simulation. As stratification increases, Re_L decreases, leading to lower available potential energy and the flow is less turbulent. A similar observation is made by Strang and Fernando (2001) and Peltier and Caulfield (2003), indicating that increasing stratification leads to a decrease in mixing efficiency, as strongly stratified flows are not greatly susceptible to flow instabilities of any kind.

5. Conclusion

Three-dimensional simulations of cylindrical gravity currents were conducted in this study where the stratification strength of the ambient fluid was varied from 0 to 0.8 at $Re = 3450$. The main objective of the study was to analyse the mixing behaviour of a fully cylindrical gravity current in a stratified ambient at a moderate Reynolds number. The mechanical energy framework allowed for the evaluation of the temporal evolution of the conversion process from available potential energy to kinetic energy through reversible stirring.

During the slumping phase, the available potential energy reaches its minimum, while the kinetic energy increases to its maximum. Subsequently, both kinetic energy and available potential energy start to decrease as the current transitions into a self-similar regime. It is worth noting that in the stratified cases, both the total potential energy and background potential energy were significantly greater than in the unstratified case. This difference can be attributed to the arrangement of stratification in the ambient, deviating from its equilibrium stable arrangement. The temporal evolution of background potential energy exhibits a higher value at the beginning of the simulation with increasing stratification strength, gradually decreasing over time.

The irreversible mixing rate for the unstratified case was higher compared to the stratified cases during the slumping phase. Both the cumulative and instantaneous mixing efficiency were plotted to measure the proportion of the kinetic energy that is irreversibly converted to background potential energy due to mixing. The results show that the Kelvin–Helmholtz billows play an important role in mixing, responsible for stirring the heavy fluid into the current and permanently mixing it with the ambient fluid. For the unstratified case, the flow is more turbulent compared to stratified cases, in which the Kelvin–Helmholtz billows are larger, and the local Reynolds number during the slumping phase is higher with decreasing stratification strength.

In the present study, the simulations were conducted at a Reynolds number of $Re = 3450$, with the local Reynolds number during the slumping phase ranging from $1300 < Re_L < 900$. The dominant influence of the laminar diffusive process, Φ_i, is evident due to the absence of macroscopic fluid motion. This significance becomes pronounced during the gravity current's transition to the inertial phase, where the balance between the buoyancy and inertial forces occurs. In the inertial phase, the local Reynolds number decreases compared to the slumping phase due to the decrease in front velocity, with an exponent of $-1/2$ (Lam et al., 2024). Furthermore, the fluid in the tail of the gravity current hardly moving (or remains stagnant), leading to an increase in Φ_i as the average density at the bottom boundary becomes greater than that at the top boundary. This increase in Φ_i results in an increase in P.

These findings contribute to a better understanding of the dynamics of gravity currents in stratified environments and have practical implications for natural phenomena such as the transport and mixing of smoke and bushfire. Further investigations could explore the effect of different lock aspect ratios on the mixing of gravity currents in stratified ambients, providing additional insights for real-world applications.

CRediT authorship contribution statement

Wai Kit Lam: Writing – review & editing, Writing – original draft, Visualization, Validation, Software, Methodology, Investigation, Formal analysis, Conceptualization. **Leon Chan:** Writing – review & editing, Supervision, Methodology, Conceptualization. **Yicheng Cao:** Validation, Software, Methodology, Conceptualization. **Duncan Sutherland:** Writing – review & editing, Supervision, Resources, Conceptualization. **Richard Manasseh:** Writing – review & editing, Supervision, Resources, Conceptualization. **Khalid Moinuddin:** Writing – review & editing, Supervision, Resources, Conceptualization. **Andrew Ooi:** Writing – review & editing, Visualization, Supervision, Resources, Methodology, Funding acquisition, Conceptualization.

Declaration of competing interest

The authors declare the following financial interests/personal relationships which may be considered as potential competing interests: Andrew Ooi reports financial support was provided by Australian Research Council.

Data availability

Data will be made available on request.

Acknowledgements

References

Agrawal, T., Ramesh, B., Zimmerman, S.J., Philip, J., Klewicki, J.C., 2021. Probing the high mixing efficiency events in a lock-exchange flow through simultaneous velocity and temperature measurements. Phys. Fluids 33 (1).

Alahyari, A.A., Longmire, E.K., 1996. Development and structure of a gravity current head. Exp. Fluids 20 (6), 410–416.

Birman, V.K., Martin, J.E., Meiburg, E., 2005. The non-Boussinesq lock-exchange problem. Part 2. High-resolution simulations. J. Fluid Mech. 537, 125–144.

Birman, V.K., Meiburg, E., Ungarish, M., 2007. On gravity currents in stratified ambients. Phys. Fluids 19 (8), 086602.

Blanchette, F., Strauss, M., Meiburg, E., Kneller, B., Glinsky, M.E., 2005. High-resolution numerical simulations of resuspending gravity currents: Conditions for self-sustainment. J. Geophys. Res. Oceans 110 (C12), 1–15.

Bonometti, T., Balachandar, S., 2008. Effect of Schmidt number on the structure and propagation of density currents. Theor. Comput. Fluid Dyn. 22 (5), 341–361.

Cantero, M.I., Balachandar, S., García, M.H., 2007a. High-resolution simulations of cylindrical density currents. J. Fluid Mech. 590, 437–469.

Cantero, M.I., Balachandar, S., García, M.H., Bock, D., 2008. Turbulent structures in planar gravity currents and their influence on the flow dynamics. J. Geophys. Res. Oceans 113 (C8), 1–22.

Cantero, M.I., Lee, J.R., Balachandar, S., García, M.H., 2007b. On the front velocity of gravity currents. J. Fluid Mech. 586, 1–39.

Cao, Y., Ooi, A., Philip, J., 2024. Characteristics of planar buoyant jets and plumes in a turbulent channel crossflow from direct numerical simulations. Environ. Fluid Mech. 1–28.

Cao, Y., Philip, J., Ooi, A., 2022. Characteristics of a buoyant plume in a channel with cross-flow. Int. J. Heat Fluid Flow 93, 108899.

Dai, A., 2015. High-resolution simulations of downslope gravity currents in the acceleration phase. Phys. Fluids 27 (7), 076602.

Dai, A., Huang, Y.L., Hsieh, Y.M., 2021. Gravity currents propagating at the base of a linearly stratified ambient. Phys. Fluids 33 (6), 066601.

Dold, J.W., Zinoviev, A., Weber, R.O., 2006. Nonlocal flow effects in bushfire spread rates.

Fischer, P.F., Lottes, J.W., Kerkemeier, S.G., 2008. nek5000 web page. URL http://nek5000.mcs.anl.gov.

Fragoso, A.T., Patterson, M.D., Wettlaufer, J.S., 2013. Mixing in gravity currents. J. Fluid Mech. 734, R2.

Gregg, M.C., D'Asaro, E.A., Riley, J.J., Kunze, E., 2018. Mixing efficiency in the ocean. Annu. Rev. Mar. 10, 443–473.

Härtel, C., Meiburg, E., Necker, F., 2000. Analysis and direct numerical simulation of the flow at a gravity-current head. Part 1. Flow topology and front speed for slip and no-slip boundaries. J. Fluid Mech. 418, 189–212.

Huppert, H.E., Simpson, J.E., 1980. The slumping of gravity currents. J. Fluid Mech. 99 (4), 785–799.

Ilıcak, M., 2014. Energetics and mixing efficiency of lock-exchange flow. Ocean Model. 83, 1–10.

Lam, W., Chan, L., Hasini, H., Ooi, A., 2018a. An analysis of two-dimensional stratified gravity current flow using open FOAM. Int. J. Eng. Technol. (UAE) 7, 589–595.

Lam, W., Chan, L., Hasini, H., Ooi, A., 2018b. Direct numerical simulation of two-dimensional stratified gravity current flow with varying stratification and aspect ratio. In: 21st Australasian Fluid Mechanics Conference. pp. 1–5.

Lam, W., Chan, L., Hasini, H., Ooi, A., 2022a. Numerical simulation of the cylindrical release gravity current in a stratified ambient. In: 23rd Australasian Fluid Mechanics Conference. pp. 1–8.

Lam, W.K., Chan, L., Ooi, A., 2022b. Numerical study of the dynamics of stratified gravity current. In: Proceedings of the 12th Australasian Heat and Mass Transfer Conference. pp. 1–8.

Lam, W.K., Chan, L., Sutherland, D., Manasseh, R., Moinuddin, K., Ooi, A., 2024. Effect of stratification on the propagation of a cylindrical gravity current. J. Fluid Mech. 983, A43.

Marino, B.M., Thomas, L.P., Linden, P.F., 2005. The front condition for gravity currents. J. Fluid Mech. 536, 49–78.

Maxworthy, T., Leilich, J., Simpson, J.E., Meiburg, E.H., 2002. The propagation of a gravity current into a linearly stratified fluid. J. Fluid Mech. 453, 371–394.

Meiburg, E., Radhakrishnan, S., Nasr-Azadani, M., 2015. Modeling gravity and turbidity currents : computational approaches and challenges. Appl. Mech. Rev. 67 (4), 040802.

Mukherjee, P., Balasubramanian, S., 2021. Diapycnal mixing efficiency in lock-exchange gravity currents. Phys. Rev. Fluids 6 (1), 013801.

Necker, F., Härtel, C., Kleiser, L., Meiburg, E., 2005. Mixing and dissipation in particle-driven gravity currents. J. Fluid Mech. 545, 339–372.

Ng, C.S., Ooi, A., Chung, D., 2016. Potential energy in vertical natural convection. In: 20th Australasian Fluid Mechanics Conference. pp. 1–4.

Ottolenghi, L., Adduce, C., Inghilesi, R., Armenio, V., Roman, F., 2016. Entrainment and mixing in unsteady gravity currents. J. Hydraul. Res. 54 (5), 541–557.

Ottolenghi, L., Adduce, C., Roman, F., Armenio, V., 2017. Analysis of the flow in gravity currents propagating up a slope. Ocean Model. 115, 1–13.

Parsons, J.D., 2000. Are fast-growing martian dust storms compressible? Geophys. Res. Lett. 27 (15), 2345–2348.

Patterson, M.D., Caulfield, C.P., McElwaine, J.N., Dalziel, S.B., 2006. Time-dependent mixing in stratified Kelvin-Helmholtz billows: Experimental observations. Geophys. Res. Lett. 33 (15).

Peltier, W.R., Caulfield, C.P., 2003. Mixing efficiency in stratified shear flows. Annu. Rev. Fluid Mech. 35 (1), 135–167.

Salehipour, H., Peltier, W.R., 2015. Diapycnal diffusivity, turbulent Prandtl number and mixing efficiency in Boussinesq stratified turbulence. J. Fluid Mech. 775 (464–500).

Simpson, J.E., 1982. Gravity currents in the laboratory, atmosphere, and ocean. Annu. Rev. Fluid Mech. 22 (1), 213–234.

Strang, E.J., Fernando, H.J.S., 2001. Entrainment and mixing in stratified shear flows. J. Fluid Mech. 428 (349–386).

Turnbull, B., McElwaine, J.N., 2007. A comparison of powder-snow avalanches at Vallée de la Sionne, Switzerland, with plume theories. J. Glaciol. 53 (180), 30–40.

Turner, J.S., 1979. Buoyancy Effects in Fluids. Cambridge University Press, Cambridge.

Ungarish, M., Huppert, H.E., 2002. On gravity currents propagating at the base of a stratified ambient. J. Fluid Mech. 458, 283–301.

Ungarish, M., Huppert, H.E., 2006. Energy balances for propagating gravity currents: homogeneous and stratified ambients. J. Fluid Mech. 565, 363–380.

Ungarish, M., Huppert, H.E., 2008. Energy balances for axisymmetric gravity currents in homogeneous and linearly stratified ambients. J. Fluid Mech. 616, 303–326.

Venayagamoorthy, S.K., Koseff, J.R., 2016. On the flux Richardson number in stably stratified turbulence. J. Fluid Mech. 10, R1.

Winters, K.B., Lombard, P.N., Riley, J.J., D'Asaro, E.A., 1995. Available potential energy and mixing in density-stratified fluids. J. Fluid Mech. 289, 115–128.

Zahtila, T., Lam, W.K., Chan, L., Sutherland, D., Moinuddin, K., A., D., T. Skvortsov, A., Manasseh, R., Ooi, A., 2024. On the propagation of planar gravity currents into a stratified ambient. Phys. Fluids 36 (3), 036601.

Zahtila, T., Lu, W., Chan, L., Ooi, A., 2023. A systematic study of the grid requirements for a spectral element method solver. Comput. & Fluids 251, 105745.